

# WaveBench: Benchmarks Datasets for Modeling Wave Propagation PDEs

Anonymous authors

Paper under double-blind review

## Abstract

Wave-based imaging techniques play a critical role in diverse scientific, medical, and industrial endeavors, from discovering hidden structures beneath the Earth’s surface to ultrasound diagnostics. They rely on accurate solutions to the forward and inverse problems for partial differential equations (PDEs) that govern wave propagation. Surrogate PDE solvers based on machine learning emerged as an effective approach to computing the solutions more efficiently than via classical numerical schemes. However, existing datasets for PDE surrogates offer only limited coverage of the wave propagation phenomenon. In this paper, we present WAVEBENCH, a comprehensive collection of benchmark datasets for wave propagation PDEs. WAVEBENCH **(1)** contains 24 datasets that cover a wide range of forward and inverse problems for time-harmonic and time-varying wave phenomena; **(2)** includes a user-friendly PyTorch environment for comparing learning-based methods; and **(3)** comprises reference performance and model checkpoints of popular PDE surrogates such as Fourier neural operators and U-Nets. Our evaluation on WAVEBENCH demonstrates the impressive performance of PDE surrogates on *in-distribution* samples, while simultaneously unveiling their limitations on *out-of-distribution* samples, indicating room for future improvements. We anticipate that WAVEBENCH will stimulate the development of accurate wave-based imaging techniques through machine learning.

## 1 Introduction

Waves are behind imaging modalities as diverse as reflection seismology, medical ultrasound, and X-ray crystallography. Imaging with waves relies on mathematical models of wave propagation expressed through partial differential equations (PDEs) called wave equations.

Since conventional numerical PDE solvers are computationally expensive for large-scale problems, recent research has witnessed a rapid emergence of machine learning-based models to approximate PDE solutions (Li et al., 2020; Nelsen & Stuart, 2021; Lu et al., 2019; Bhattacharya et al., 2021; Li et al., 2021; Huang et al., 2021; Wang et al., 2021; Gupta et al., 2021; de Hoop et al., 2022a; Kissas et al., 2022; Brandstetter et al., 2023). These models, collectively referred to as *PDE surrogates*, are trained using a dataset of ground-truth PDE solutions. Properly trained PDE surrogates can offer faster inference speeds compared to traditional numerical solvers while maintaining accuracy. Realizing this advantage, however, typically requires having access to high-quality PDE solutions for training purposes.

Indeed, it is hard to overstate the significance of high-quality datasets in the success of modern machine learning models in computer vision and natural language processing. Similarly, in the case of PDE surrogates, the importance of high-quality datasets has become evident. Recent efforts focus on constructing high-quality datasets for PDE surrogates (Lu et al., 2022; de Hoop et al., 2022b; Gupta & Brandstetter, 2022; Takamoto et al., 2022). These datasets cover a wide range of equations, especially those related to fluid dynamics, such as Darcy flow, shallow-water, and Navier–Stokes equations (Li et al., 2021; Gupta & Brandstetter, 2022; Stachenfeld et al., 2022; Holl et al., 2020). However, a comprehensive dataset for a broad family of wave PDEs is still missing.

To address the gap, we present WAVEBENCH, an extensive collection of benchmark datasets designed for wave propagation PDEs. WAVEBENCH includes 24 datasets, encompassing two categories of forward and inverse problems of acoustic waves: *time-harmonic problems* and *time-varying problems*. These datasets are constructed using open-source software tools `hawen` (Faucher, 2021) for time-harmonic waves and `j-wave` (Stanziola et al., 2023) for time-varying waves. We have made these datasets publicly accessible for researchers to access. Moreover, we provide a PyTorch (Paszke et al., 2019) environment that enables easy training and comparison between various PDE surrogate models. We also include checkpoints and reference results for popular PDE surrogates of Fourier neural operators (Li et al., 2021), U-Nets (Ronneberger et al., 2015), and the U-shaped neural operator (Rahman et al., 2023). By providing these resources, we aim to foster the development of machine-learning techniques for wave imaging.

## 2 Background and related work

**ML methods to approximate operators described by PDEs.** The solution map of a generic PDE can be written as an operator  $G^\dagger : \mathcal{A} \rightarrow \mathcal{U}$ , where  $\mathcal{A}$  and  $\mathcal{U}$  are normed function spaces defined on some bounded subsets in  $\mathbb{R}^d$ . We focus on 2D domains, thus  $d = 2$ . For instance,  $G^\dagger$  can be a mapping that converts PDE coefficients  $a \in \mathcal{A}$  into a PDE solution  $G^\dagger(a) \in \mathcal{U}$ . A PDE surrogate  $G_\theta$  is a data-driven emulator of the true PDE solution map  $G^\dagger$ , with  $\theta$  denoting the model parameters. A PDE surrogate is learned from a training dataset of input-output pairs  $\{(a_j, u_j)\}_{j=1}^N$ , where  $a_j \in \mathcal{A}$  and  $u_j = G^\dagger(a_j)$  are prepared using conventional numerical solvers. The *loss* quantifying how well a PDE surrogate with parameters  $\theta$  fits the data is formulated as

$$L_N(\theta) := \frac{1}{N} \sum_{j=1}^N l(G_\theta(a_j), u_j),$$

where the error function  $l(\cdot, \cdot)$  is often chosen as the absolute error  $l(\hat{u}, u) = \|\hat{u} - u\|_{\mathcal{U}}$  or the relative error  $l(\hat{u}, u) = \|\hat{u} - u\|_{\mathcal{U}} \|\hat{u}\|_{\mathcal{U}}^{-1}$  (Kovachki et al., 2023). Once trained, the model  $G_\theta$  yields approximate PDE solutions, often faster than traditional solvers.

**PDEs surrogates.** A PDE surrogate  $G_\theta$  can be parameterized in various ways. Popular choices include kernel-based models (Kadri et al., 2016; Griebel & Rieger, 2017), random feature models (Nelsen & Stuart, 2021), Gaussian processes (Chen et al., 2021), and neural networks (Lu et al., 2019; Kovachki et al., 2023; Bhattacharya et al., 2021; Wang et al., 2021; Kissas et al., 2022; Brandstetter et al., 2023). Among them, neural networks represent the current state-of-the-art in empirical performance. Recently, Lu et al. (2022); de Hoop et al. (2022b); Gupta & Brandstetter (2022); Takamoto et al. (2022) ran a comprehensive numerical comparison of various models, showing their relative merits in different scenarios. For PDEs discretized on 2D grid meshes, Fourier neural operators (FNO) and U-Nets are highly performant (Takamoto et al., 2022; Gupta & Brandstetter, 2022); we thus adopt them as baselines.

**Benchmarks and datasets for PDEs surrogates.** Recent advancements in PDE surrogates have led to the development of standardized datasets that serve as benchmarks (Lu et al., 2019; Kothari et al., 2020; Li et al., 2021; Lu et al., 2022; de Hoop et al., 2022b; Gupta & Brandstetter, 2022; Takamoto et al., 2022; Benitez et al., 2023). These datasets comprise a wide range of PDEs, usually with particular emphasis on fluid dynamics problems such as Darcy flow, shallow-water, and Navier–Stokes problems. Despite this impressive variety, there is a noticeable gap in the coverage of wave propagation PDEs. While a few work apply PDE surrogates on wave problems (Kothari et al., 2020; de Hoop et al., 2022b; Deng et al., 2022; Benitez et al., 2023), each focuses on a specialized setting. For instance, Kothari et al. (2020) and Deng et al. (2022) focus on certain time-varying wave problems, and Stanziola et al. (2021); de Hoop et al. (2022b) and Benitez et al. (2023) concentrate on time-harmonic ones. In contrast, the proposed WAVEBENCH provides a comprehensive range of wave propagation datasets by considering both time-varying and time-harmonic problems. Additionally, we cover a wide range of frequency configurations for time-harmonic problems and take different types of wave speeds into account for both time-varying and time-harmonic problems. To facilitate model comparisons, we also offer a unified PyTorch environment for comparing and benchmarking models.

### 3 WaveBench datasets

Our proposed WAVEBENCH consists of 20 datasets, divided into two problem categories: time-harmonic wave problems and time-varying problems.

#### 3.1 Datasets for time-harmonic wave problems

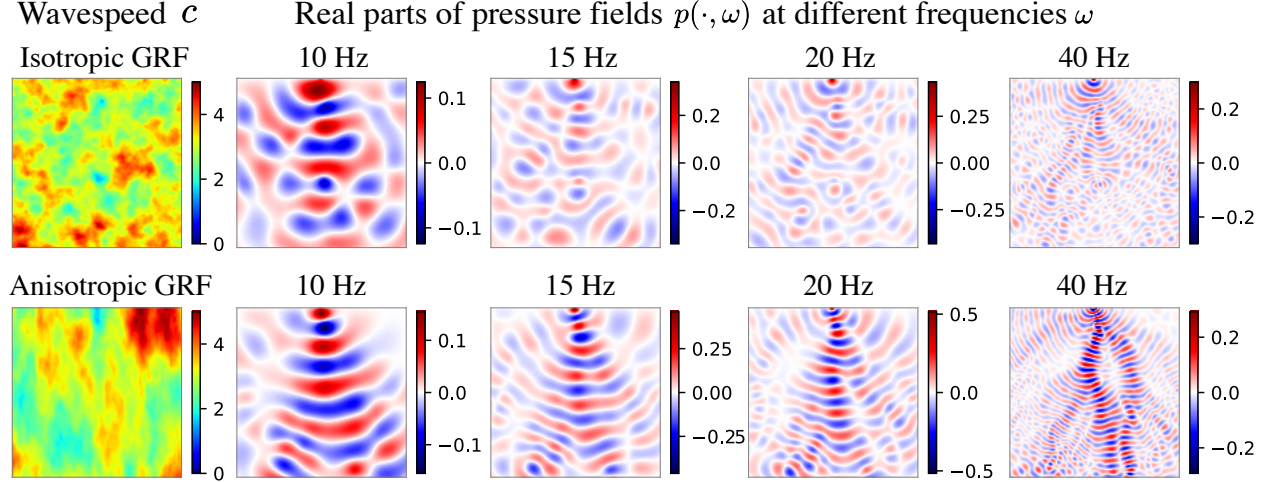


Figure 1: **Visualization of samples from the acoustic time-harmonic datasets.** At a fixed frequency  $\omega$ , the solver to the Helmholtz equation (1) converts a wavespeed  $c$  to a pressure field  $p(\cdot, \omega)$ . Two wavespeed  $c$  are shown in the left-most panels. They are realizations of Gaussian random field (GRF) with an isotropic kernel and an anisotropic kernel, respectively. The right panels display ground-truth pressure field  $p(\cdot, \omega)$  at frequencies  $\omega/(2\pi) = 10\text{Hz}, 15\text{Hz}, 20\text{Hz},$  and  $40\text{Hz}$ .

The time-harmonic wave equation describes wave phenomena in the frequency domain. We consider the propagation of time-harmonic acoustic waves as well as time-harmonic elastic waves.

**Time-harmonic acoustic waves.** The propagation of time-harmonic acoustic waves is described by the Helmholtz equation:

$$-\left(\Delta + \frac{\omega^2}{c(\mathbf{x})^2}\right)p(\mathbf{x}, \omega) = f(\mathbf{x}, \omega), \quad (1)$$

where  $p = p(\mathbf{x}, \omega)$  is a pressure field at the angular frequency  $\omega$ ,  $c$  is a wavespeed function, and  $f$  is a point source function; throughout this work, our domain is in 2D, that is,  $\mathbf{x} \in \mathbb{R}^2$ . Figure 1 provides an illustration of the wavespeed  $c$  and pressure field  $p$ . The boundary conditions in our study are detailed in Appendix C.

At a fixed frequency  $\omega$  and source  $f$ , the parametric form of the Helmholtz equation describes an operator  $G_{\text{helm}}^\dagger$  that maps the wavespeed  $c$  to a pressure field  $p$ :

$$G_{\text{helm}}^\dagger : c \mapsto p(\cdot, \omega). \quad (2)$$

To estimate the operator  $G_{\text{helm}}^\dagger$  from data, we construct datasets that contain paired wavespeed and pressure field  $\{(c_j, p_j)\}_j$ . We let the wavespeed  $c$  be realizations of Gaussian random fields (GRF) with an isotropic kernel or an anisotropic kernel. For each wavespeed  $c$ , the corresponding ground truth pressure field  $p$  is obtained by solving the PDE using a hybridizable discontinuous Galerkin (HDG) method (Faucher & Scherzer, 2020) implemented in `hawen` package (Faucher, 2021). We produce 8 time-harmonic datasets corresponding to 2 wavespeed types and 4 frequencies. Each dataset contains 49,000 training samples, 500 validation samples, and 500 test samples. For an overview of these time-harmonic datasets, please refer to Table 2 of Appendix A.

**Time-harmonic elastic waves.** Unlike the acoustic wave problem which models a scalar pressure field, the elastic case works with the displacement vector field  $\mathbf{u}$ , written as  $\mathbf{u} = [\mathbf{u}_x, \mathbf{u}_y]$  in 2D. Each component ( $\mathbf{u}_x$  or  $\mathbf{u}_y$ ) is complex-valued. Furthermore, a wave in an elastic medium is associated with two wavespeed functions  $c_p$  and  $c_s$ , corresponding to the P-wave (compressional or primary wave) and S-wave (shear or secondary wave). We visualize the wavespeeds and the real parts of the displacement fields at different frequencies in Figure 2. More details of our time-harmonic elastic datasets are provided in Appendix A.2.

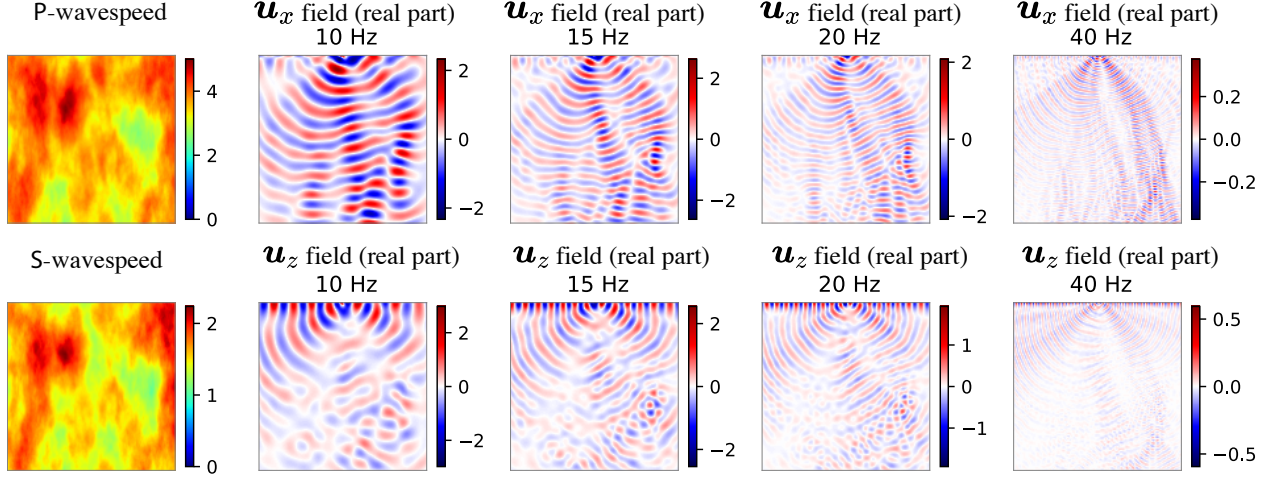


Figure 2: **Visualization of samples from the elastic time-harmonic datasets.** The wavespeeds are separated into P-waves and S-waves shown in the left-most column. At a fixed frequency  $\omega$ , the solver converts wavespeed  $c$  to a displacement field  $\mathbf{u} = [\mathbf{u}_x, \mathbf{u}_z]$ . The right panels display these displacement fields at frequencies  $\omega/(2\pi) = 10\text{Hz}, 15\text{Hz}, 20\text{Hz},$  and  $40\text{Hz}$ .

### 3.2 Datasets for time-varying wave problems

We now turn to the governing equation for acoustic wave propagation in the time domain. The acoustic wave equation describes the evolution of pressure  $q = q(\mathbf{x}, t)$  over time under the influence of the wavespeed  $c = c(\mathbf{x})$ :

$$\Delta q(\mathbf{x}, t) - \frac{1}{c(\mathbf{x})^2} \frac{\partial^2 q(\mathbf{x}, t)}{\partial t^2} = 0 \quad (3)$$

This equation is subject to radiating boundary conditions detailed in Appendix B. The time-varying quantity  $q = q(\mathbf{x}, t)$  in (3) and the time-harmonic quantity  $p = p(\mathbf{x}, \omega)$  in (1) are related: under appropriate assumptions,  $q(\mathbf{x}, t)$  can be written as an integration of  $p(\mathbf{x}, \omega)$  in the frequency domain. We consider two problems that arise from the time-varying wave dynamics: the *reverse time continuation* and the *inverse source* problem.

**Reverse time continuation (RTC) problem.** The goal of this problem is to determine the initial pressure of the wave equation (3) based on the final pressure. Let  $q(\cdot, 0)$  be the initial pressure, which propagates over a time span  $T$  to reach the final pressure  $q(\cdot, T)$ . Note that the final pressure  $q(\cdot, T)$  is influenced by both the initial pressure  $q(\cdot, 0)$  and the wavespeed  $c$  in (3). With wavespeed  $c$  fixed, the ground-truth operator that solves the RTC task is represented by

$$G_{\text{rtc}}^\dagger : q(\cdot, T) \mapsto q(\cdot, 0). \quad (4)$$

We construct the RTC dataset in the form of  $(q_j(\cdot, T), q_j(\cdot, 0))_j$ , with a fixed propagation time  $T$  but different wavespeed types. Figure 3 illustrates samples from these datasets. We consider three types of wavespeed  $c$  (top panels of Figure 3): Gaussian lens and realizations of isotropic and anisotropic Gaussian random fields. For configuring the initial pressure  $q(\cdot, 0)$ , we use two approaches. In the first approach, we place

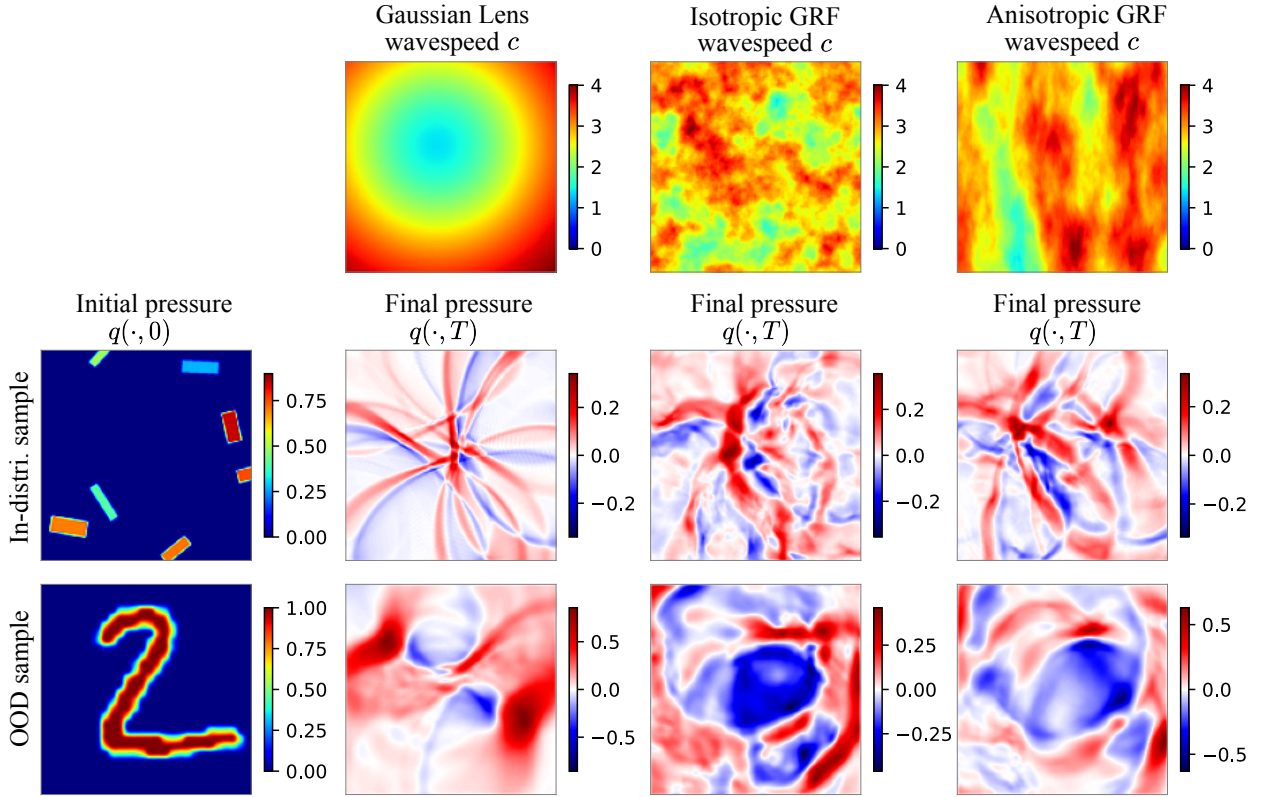


Figure 3: **Visualization of samples from the reverse time continuation (RTC) problems.** With a fixed wavespeed  $c$ , the goal of RTC is to map the final pressure  $q(\cdot, T)$  to the initial pressure  $q(\cdot, 0)$ . The top-most panels depict three types of wavespeeds  $c$ . The left-most panels depict two realizations of initial pressures  $q(\cdot, 0)$ . The remaining panels display the final pressures  $q(\cdot, T)$ , which are influenced by both the initial pressure  $q(\cdot, 0)$  in its respective row and the wavespeed  $c$  in its corresponding column.

boxes or thick lines of random sizes, orientations, and locations in the domain, following the approach in [Kothari et al. \(2020\)](#). Additionally, to evaluate the out-of-distribution (OOD) generalization performance of models, we construct test datasets using MNIST images ([LeCun et al., 1998](#)) as the initial pressure. The two bottom rows of Figure 3 display samples from both the in-distribution thick line initial pressure and the OOD MNIST pressure. Appendix B provides detailed configuration information about the RTC datasets.

**Inverse source (IS) problem.** In the previous RTC problem, we are given the final pressure  $q(\cdot, T)$  on the full domain at a terminal time  $T$ . However, this assumption is often too strong in applications such as seismic imaging, where the pressure can only be measured by sensors placed at some portions of the domain boundary. To address this limitation, we turn to the inverse source (IS) problem. The IS problem aims to predict the initial pressure  $q(\cdot, 0)$  based on pressure measurements taken at certain boundary locations over a time span  $[0, T]$ . Given a fixed wavespeed  $c$ , sensor locations  $S$ , and discrete time steps  $\mathcal{T}$ , the ground-truth operator that solves the IS task can be expressed as:

$$G_{\text{is}}^{\dagger} : [q(\mathbf{x}, t)]_{\mathbf{x} \in S, t \in \mathcal{T}} \mapsto q(\cdot, 0). \quad (5)$$

This problem is illustrated in Figure 4. Similar to the RTC dataset, we create random thick lines and use them as initial pressure  $q(\cdot, 0)$ . In Figure 4, we visualize samples from IS datasets. The sensor locations  $S$  are fixed to be the upper boundary of the domain. Further details on the configuration of the IS datasets are provided in Appendix B.

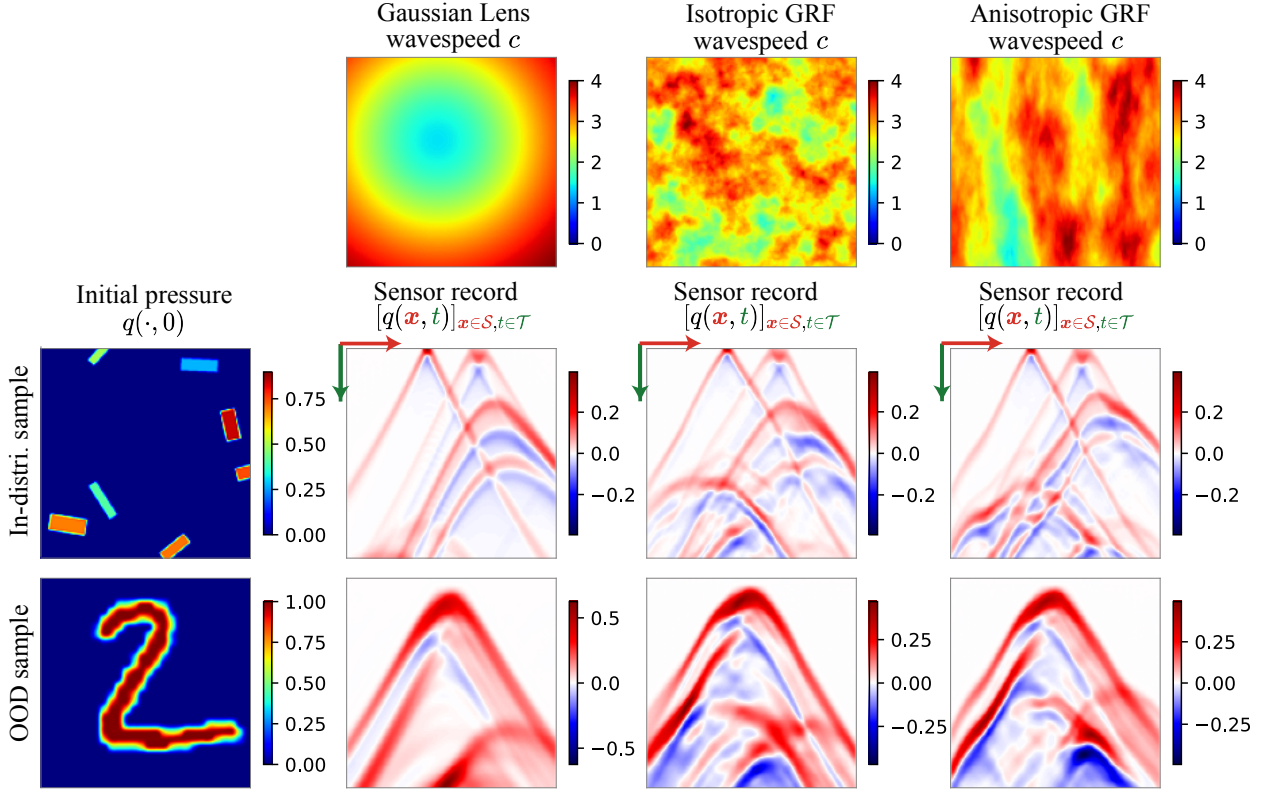


Figure 4: **Visualization of samples from the inverse source (IS) problems.** At a fixed wavespeed  $c$ , the goal of IS is to map  $[q(\mathbf{x}, t)]_{\mathbf{x} \in \mathcal{S}, t \in \mathcal{T}}$  (pressure recorded at sensor locations  $\mathcal{S}$  and time  $\mathcal{T}$ ) into the initial pressure  $q(\cdot, 0)$ . The top-most panels depict three types of wavespeeds  $c$ . The left-most panels depict two realizations of initial pressures  $q(\cdot, 0)$ . The remaining panels exhibit the sensor records  $[q(\mathbf{x}, t)]_{\mathbf{x} \in \mathcal{S}, t \in \mathcal{T}}$ , which are influenced by both the initial pressure  $q(\cdot, 0)$  in its respective row and the wavespeed  $c$  in its corresponding column.

We summarize our 12 time-varying datasets of RTC and IS in Table 3 in Appendix B. Each dataset based upon the initial pressures of thick lines consists of 9,000 training samples, 500 validation samples, and 500 testing samples. Each dataset based upon the initial pressures of MNIST is for out-of-distribution testing purposes, comprising of 500 testing samples.

### 3.3 Dataset accessibility and format.

The datasets are in the `beton` format of FFCV (Leclerc et al., 2023), which is an open-source software that provides high-throughput data loading for model training. Our datasets will be accessible on Zenodo (an open platform for datasets sharing), and the benchmark code will be accessible through our GitHub repository; links to both will be provided here upon the de-anonymization of our submission.

## 4 Wavebench Benchmarks

### 4.1 Baseline models

We provide reference implementations and benchmark performance of PDE surrogates trained on WAVEBENCH datasets. We focus on U-Nets and FNOs as PDE surrogates, which exhibit high performance across various PDE problems (Takamoto et al., 2022; Gupta & Brandstetter, 2022).

Model	# parameters	Forward pass runtime [s]	Backward pass runtime [s]
FNO-depth-4	4.2M	0.011	0.018
FNO-depth-8	8.4M	0.019	0.033
U-Net-ch-32	7.8M	0.006	0.012
U-Net-ch-64	31.0M	0.016	0.031
UNO-modes-12	10.1M	0.024	0.032
UNO-modes-16	17.9M	0.024	0.033

Table 1: **Comparison of baseline models.** The baseline models include two variants of FNO (Li et al., 2021) and two variants of U-Net (Ronneberger et al., 2015). FNO-depth-4 and FNO-depth-8 are two FNO variants with of 4 or 8 hidden Fourier layers. U-Net-ch-64 stands for the standard U-Net that has 64 channels in its first layer, and U-Net-ch-32 is a smaller variant with all convolutional channels halved. Both UNO-modes-12 and UNO-modes-16 variants have 3 scales that correspond to domain-discretization of  $128 \times 128$ ,  $64 \times 64$ , and  $32 \times 32$ . The UNO-modes-12 model uses  $[12, 6, 3]$  Fourier modes for each scale, while the UNO-modes-16 uses  $[16, 8, 4]$  Fourier modes for each scale. The model runtime was assessed using a batch  $(8, 1, 128, 128)$ , consisting of 8 samples of  $128 \times 128$  array. The benchmarking procedure involved initial 10 dry runs followed by 100 test runs conducted on an 11 GB NVIDIA GeForce RTX 2080 Ti GPU.

**FNO.** The Fourier neural operator (Li et al., 2021) represents one of the state-of-the-art models for PDE data on regular grids. We use FNOs in 2D consisting of 64 hidden channels, 16 Fourier modes, and either 4 or 8 Fourier layers as hidden layers; for the input lifting and output projection parts of FNOs, we use single-hidden-layer MLPs that consisted of  $1 \times 1$  convolution with 128 channels. The FNO variants with 4 and 8 hidden Fourier layers are referred to as FNO-depth-4 and FNO-depth-8, whose parameter count and runtime are summarized in Table 1.

**U-Net.** The U-Net (Ronneberger et al., 2015) is a convolutional network originally developed for 2D image-to-image regression problems such as image segmentation. However, its versatility has led to its adoption in PDE learning tasks (Kothari et al., 2020; Li et al., 2021; Gupta & Brandstetter, 2022; Chen & Thuerey, 2023), both as a component within larger architectures or as standalone model. Remarkably, even as a standalone model, U-Nets perform well in several PDE modeling tasks, sometimes matching or surpassing dedicated PDE surrogates such as FNOs (Takamoto et al., 2022; Gupta & Brandstetter, 2022). In our baselines, we employ either the standard U-Net (Ronneberger et al., 2015), referred to as U-Net-ch-64 as it uses 64 channels in the first hidden layer, or a smaller variant with halved convolutional channels (referred to as U-Net-ch-32). Table 1 summarizes their parameter counts and runtime.

**UNO.** The UNO (U-shaped neural operator) (Rahman et al., 2023) combines U-Net and FNO design elements. Like U-Net, UNO encodes input into smaller domains and decodes to generate output on greater domains. UNO’s layers are parametrized with Fourier layers in a way identical to FNOs. We consider two UNO variants, UNO-modes-12 and UNO-modes-16. For both versions, we use 3 scales on domains  $128 \times 128$ ,  $64 \times 64$ , and  $32 \times 32$ . UNO-modes-12 uses Fourier modes of  $[12, 6, 3]$  for each scale, and UNO-modes-16 with  $[16, 8, 4]$  for each scale.

**Training protocol.** We trained and tested the baseline U-Net, FNO, and UNO models using the 20 datasets described in Section 3 and summarized in Table 2 and Table 3 in the appendix. For all datasets, we trained all models for 50 epochs using the AdamW optimizer (Loshchilov & Hutter, 2019). The learning rates were initially set to  $1e-3$  and then annealed to  $1e-5$  using the cosine annealing (Loshchilov & Hutter, 2017). We employed the relative L2 loss for training and evaluation in all our problems, following the approach in Li et al. (2021); de Hoop et al. (2022b). Since all datasets were divided into training, validation, and test splits, we monitored the model’s generalization performance on the validation split during training. We selected the model that performed the best on the validation split for the evaluation of the test split. All experiments were conducted on an 11 GB NVIDIA GeForce RTX 2080 Ti GPU.

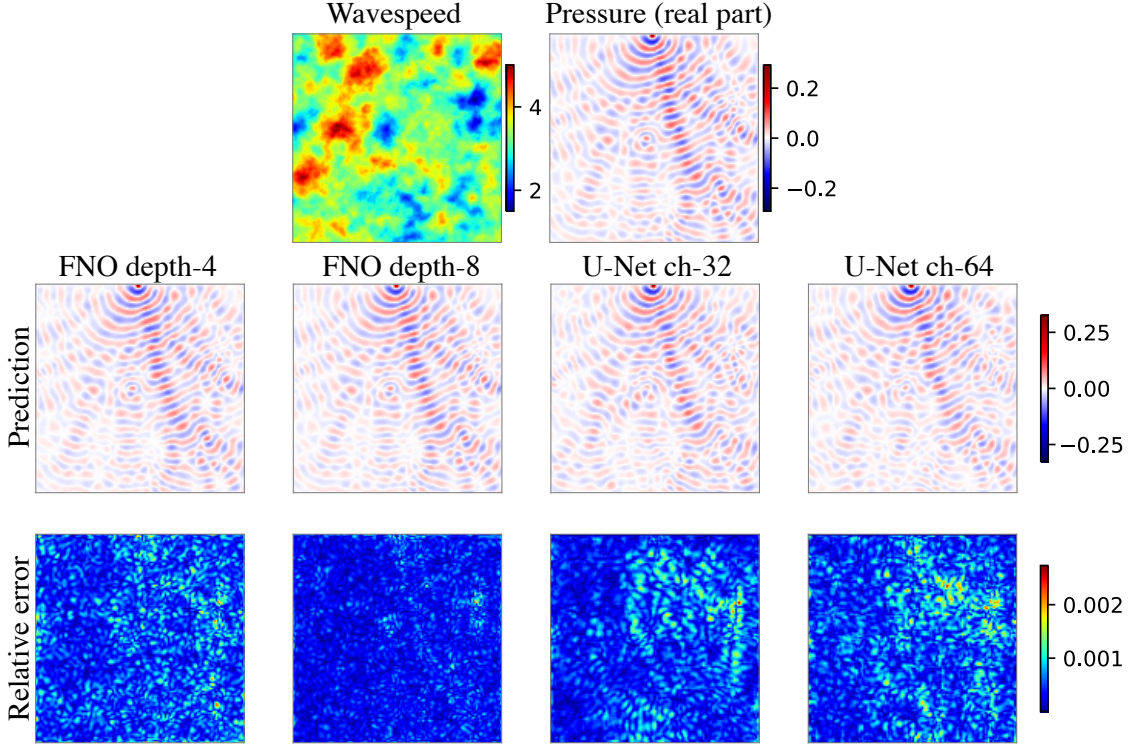


Figure 5: **In-distribution test performance of models on a acoustic time-harmonic dataset.** The model is trained and tested on splits of the acoustic time-harmonic dataset with isotropic GRF wavespeed and frequency  $\omega/2\pi = 40\text{Hz}$ . The input wavespeed  $c$  and real part of the ground-truth pressure field are shown in the top panels, cf. Equation (1). The middle panels show the predictions from 4 different models. The bottom panels show the relative error  $|p(\cdot, \omega) - \hat{p}(\cdot, \omega)| / \|p(\cdot, \omega)\|_{L^2}$  between the predicted pressure  $\hat{p}$  and the ground-truth pressure  $p$ .

In the following sections, we present empirical results on a subset of WAVEBENCH datasets. Additional visualizations and complete qualitative results are provided in Appendix A and B. Due to space limitations, we present results for PDE surrogates of FNOs and U-Nets here in the main text; UNO variant outcomes are in the appendix. In most experiments, UNOs outperform some U-Nets but not the best FNOs.

## 4.2 Performance of baseline models on time-harmonic datasets

**In-distribution performance.** Figure 5 illustrates the performances of models applied to the time-harmonic dataset with isotropic GRF wavespeeds and frequency 40 Hz. All models are trained using the training split of the dataset; the figure presents results based on a sample from the test split. All PDE surrogates produce visually comparable predictions. However, the error fields (the third row of Figure 5) show that two FNO variants produce smaller errors in comparison to U-Nets.

Numerical values of the errors are provided in Table 4 in the Appendix C.

**Out-of-distribution (OOD) performance.** While FNOs and U-Nets produce both visually and numerically appealing results for in-distribution samples, their out-of-distribution (OOD) test results clearly indicate room for further improvements (Figure 6). In this experiment, we trained models on a time-harmonic dataset with *isotropic* GRF wavespeed and evaluated them on the *anisotropic* version of the dataset. This setup presents a greater challenge, as models that can successfully solve it presumably must capture a greater extent of the physics of wave propagation. The results demonstrate that PDE surrogates generally perform

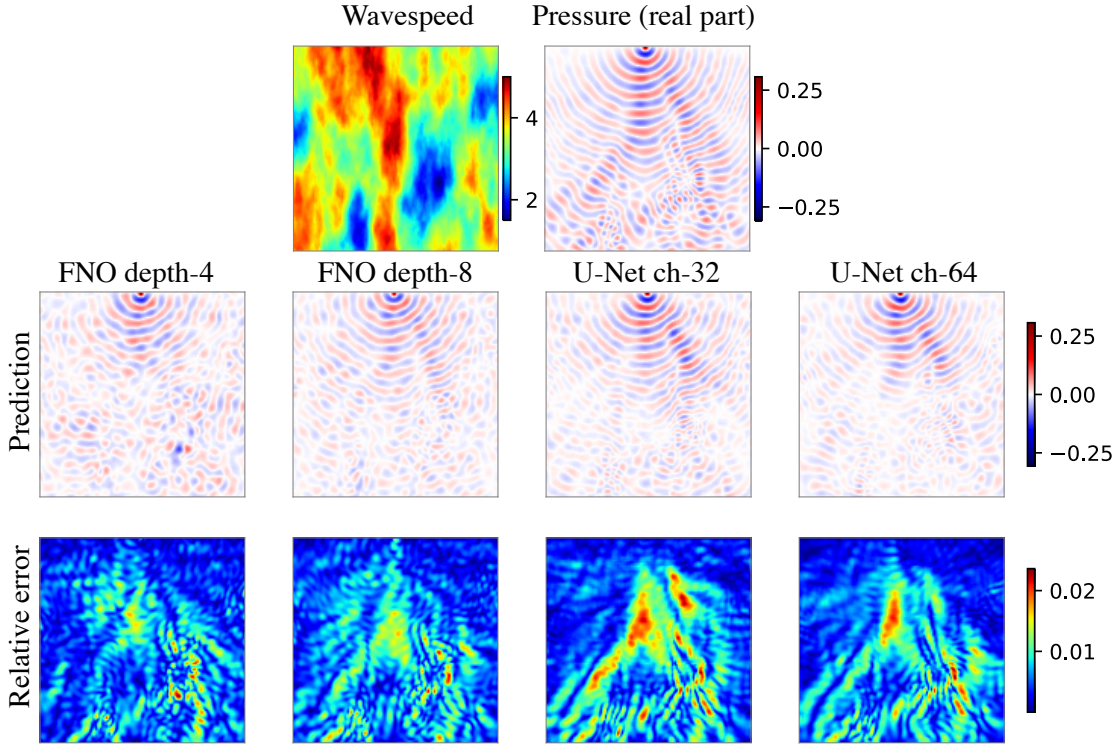


Figure 6: **OOD test performance of models on an acoustic time-harmonic dataset.** Here, the model is trained on the time-harmonic dataset with *isotropic* GRF wavespeed and frequency  $\omega/2\pi = 40\text{Hz}$ , but tested on the *anisotropic* version instead.

over 5 times worse in OOD tests compared to in-distribution tests in the metric of relative L2 error (Table 5 in the Appendix C).

### 4.3 Performance of baseline models on time-harmonic datasets

Recall that WAVEBENCH contains two time-varying wave problems: reverse time continuation (RTC) and the inverse source problem (IS). Here in the main text, we report the model performances on the more challenging IS problem. Full results of both problems can be found in Appendix E.

Figure 7 provides a visual performances comparison of PDE surrogates on the IS dataset that uses isotropic Gaussian Random Field (GRF) wavespeeds. Both U-Nets and Fourier neural operators yield comparable results on in-distribution samples. U-Nets slightly exceed FNOs in performance, though the margin is narrow (Table 7 in Appendix E). The outputs from both models are within reasonable expectations.

However, when it comes to OOD samples, both models introduce artifacts, leading to inaccuracies in reconstructing the target. This can be seen in the third row of Figure 7. There, U-Nets generate outputs with box-like patterns, which are derived from the training data; FNOs struggle to accurately reproduce the smooth contour of the OOD target. It is worth noting that similar artifacts can be consistently observed across all time-varying datasets (Appendix E).

## 5 Discussion

This paper introduces WAVEBENCH, a comprehensive repository of 24 benchmark datasets designed for wave PDEs. The datasets cover a broad range of wave-related problems, including time-dependent problems derived from the wave equation and time-harmonic problems derived from the Helmholtz equation.

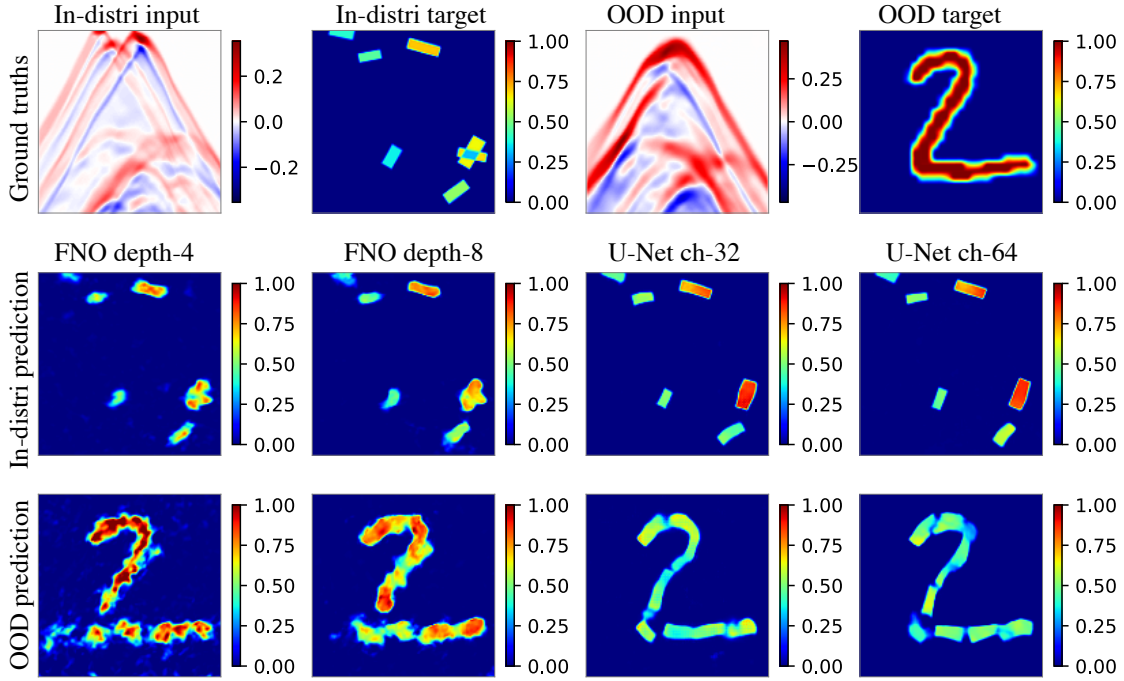


Figure 7: **Test performance of models on the time-varying IS dataset with isotropic GRF wavespeed.** The first row shows the input and target samples of the IS dataset; they can be either in-distribution or OOD. The second row shows the model predictions on the in-distribution sample. The third row shows the model predictions on the OOD sample.

WAVEBENCH serves two purposes: providing a data source for machine learning for wave problems and providing a user-friendly PyTorch environment for training and evaluating PDE surrogate models.

After evaluating PDE surrogates on the WAVEBENCH datasets, we have identified several recurring patterns. Firstly, across all datasets, U-Nets and FNOs showed remarkable capabilities in approximating wave propagation for in-distribution data. The larger models, such as FNO-depth-8 and U-Net-ch-64, outperformed their smaller counterparts like FNO-depth-4 and U-Net-ch-32. This shows the potential advantages of employing high-capacity models to tackle challenging PDE problems, assuming the existence of abundant and high-quality PDE data.

However, the performance of PDE surrogates declines significantly when moving from in-distribution to out-of-distribution (OOD) samples. This implies that although these models learn statistical patterns from the data, they do not capture the wave-propagation physics present in the data. Given the importance of OOD generalization in the practical use of wave-based techniques in exploratory scientific applications like seismic imaging and medical imaging, future PDE surrogates that have the capability to learn wave-propagation physics from data are highly sought-after.

**Limitations.** While WAVEBENCH contains a broad range of wave propagation PDE problems, we note that all WAVEBENCH datasets are presently simulated on 2D domains. A simulation of wave propagation within a 3D domain could provide a more realistic and challenging setting for applying PDE surrogates. At the same time, preparing such a dataset is computationally much more demanding. We leave this aspect for future work.

## References

Jose Antonio Lara Benitez, Takashi Furuya, Florian Faucher, Xavier Tricoche, and Maarten V de Hoop. Fine-tuning neural-operator architectures for training and generalization. *arXiv preprint arXiv:2301.11509*,

2023. (Cited on pages 2, 14, and 15.)
- Kaushik Bhattacharya, Bamdad Hosseini, Nikola B. Kovachki, and Andrew M. Stuart. Model reduction and neural networks for parametric PDEs. *The SMAI journal of computational mathematics*, 7:121–157, 2021. (Cited on pages 1 and 2.)
- Johannes Brandstetter, Rianne van den Berg, Max Welling, and Jayesh K Gupta. Clifford neural layers for PDE modeling. In *Proceedings of the Eleventh International Conference on Learning Representations (ICLR)*, 2023. (Cited on pages 1 and 2.)
- Li-Wei Chen and Nils Thuerey. Towards high-accuracy deep learning inference of compressible flows over aerofoils. *Computers & Fluids*, 250:105707, 2023. (Cited on page 7.)
- Yifan Chen, Bamdad Hosseini, Houman Owhadi, and Andrew M Stuart. Solving and learning nonlinear PDEs with Gaussian processes. *Journal of Computational Physics*, 447:110668, 2021. (Cited on page 2.)
- Maarten de Hoop, Matti Lassas, and Christopher A Wong. Deep learning architectures for nonlinear operator functions and nonlinear inverse problems. *Mathematical Statistics and Learning*, 4(1):1–86, 2022a. (Cited on page 1.)
- Maarten V. de Hoop, Daniel Zhengyu Huang, Elizabeth Qian, and Andrew M. Stuart. The cost-accuracy trade-off in operator learning with neural networks. *Journal of Machine Learning*, 1(3):299–341, 2022b. (Cited on pages 1, 2, and 7.)
- Chengyuan Deng, Shihang Feng, Hanchen Wang, Xitong Zhang, Peng Jin, Yinan Feng, Qili Zeng, Yinpeng Chen, and Youzuo Lin. OPENFWI: Large-scale multi-structural benchmark datasets for full waveform inversion. In *Proceedings of the 35th Conference in Neural Information Processing Systems (NeurIPS)*, 2022. (Cited on page 2.)
- Björn Engquist and Andrew Majda. Absorbing boundary conditions for numerical simulation of waves. *Proceedings of the National Academy of Sciences*, 74(5):1765–1766, 1977. (Cited on page 14.)
- Florian Faucher. *Contributions to Seismic Full Waveform Inversion for Time Harmonic Wave Equations: Stability Estimates, Convergence Analysis, Numerical Experiments involving Large Scale Optimization Algorithms*. Theses, Université de Pau et des Pays de l’Adour, November 2017. (Cited on page 15.)
- Florian Faucher. hawen: time-harmonic wave modeling and inversion using hybridizable discontinuous Galerkin discretization. *Journal of Open Source Software*, 6(57):2699, 2021. (Cited on pages 2 and 3.)
- Florian Faucher and Otmar Scherzer. Adjoint-state method for hybridizable discontinuous Galerkin discretization, application to the inverse acoustic wave problem. *Computer Methods in Applied Mechanics and Engineering*, 372:113406, 2020. (Cited on page 3.)
- Michael Griebel and Christian Rieger. Reproducing kernel Hilbert spaces for parametric partial differential equations. *SIAM/ASA Journal on Uncertainty Quantification*, 5(1):111–137, 2017. (Cited on page 2.)
- Gaurav Gupta, Xiongye Xiao, and Paul Bogdan. Multiwavelet-based operator learning for differential equations. In *Proceedings of the 35th conference of Neural Information Processing Systems (NeurIPS)*, 2021. (Cited on page 1.)
- Jayesh K Gupta and Johannes Brandstetter. Towards multi-spatiotemporal-scale generalized PDE modeling. *arXiv preprint arXiv:2209.15616*, 2022. (Cited on pages 1, 2, 6, and 7.)
- Philipp Holl, Vladlen Koltun, Kiwon Um, and Nils Thuerey. Phiflow: A differentiable PDE solving framework for deep learning via physical simulations. In *NeurIPS workshop*, volume 2, 2020. (Cited on page 1.)
- Xiang Huang, Zhanhong Ye, Hongsheng Liu, Beiji Shi, Zidong Wang, Kang Yang, Yang Li, Bingya Weng, Min Wang, Haotian Chu, et al. Meta-auto-decoder for solving parametric partial differential equations. In *Proceedings of the 36th Conference on Neural Information Processing Systems (NeurIPS)*, 2021. (Cited on page 1.)

- Hachem Kadri, Emmanuel Duflos, Philippe Preux, Stéphane Canu, Alain Rakotomamonjy, and Julien Audiffren. Operator-valued kernels for learning from functional response data. *Journal of Machine Learning Research*, 17(20):1–54, 2016. (Cited on page 2.)
- Georgios Kissas, Jacob H Seidman, Leonardo Ferreira Guilhoto, Victor M Preciado, George J Pappas, and Paris Perdikaris. Learning operators with coupled attention. *Journal of Machine Learning Research*, 23(215):1–63, 2022. (Cited on pages 1 and 2.)
- Konik Kothari, Maarten de Hoop, and Ivan Dokmanić. Learning the geometry of wave-based imaging. *Proceedings of the 34th Conference on Neural Information Processing Systems (NeurIPS)*, 33:8318–8329, 2020. (Cited on pages 2, 5, 7, and 16.)
- Nikola Kovachki, Zongyi Li, Burigede Liu, Kamyar Azizzadenesheli, Kaushik Bhattacharya, Andrew Stuart, and Anima Anandkumar. Neural operator: Learning maps between function spaces with applications to PDEs. *Journal of Machine Learning Research*, 24(89):1–97, 2023. (Cited on page 2.)
- Guillaume Leclerc, Andrew Ilyas, Logan Engstrom, Sung Min Park, Hadi Salman, and Aleksander Mądry. FFCV: Accelerating training by removing data bottlenecks. In *Proceedings of the 34th IEEE/CVF Conference on Computer Vision and Pattern Recognition (CVPR)*, pp. 12011–12020, June 2023. (Cited on page 6.)
- Yann LeCun, Léon Bottou, Yoshua Bengio, and Patrick Haffner. Gradient-based learning applied to document recognition. *Proceedings of the IEEE*, 86(11):2278–2324, 1998. (Cited on page 5.)
- Zongyi Li, Nikola Kovachki, Kamyar Azizzadenesheli, Burigede Liu, Andrew Stuart, Kaushik Bhattacharya, and Anima Anandkumar. Multipole graph neural operator for parametric partial differential equations. *Proceedings of the 34th Conference on Neural Information Processing Systems (NeurIPS)*, 33, 2020. (Cited on page 1.)
- Zongyi Li, Nikola Kovachki, Kamyar Azizzadenesheli, Burigede Liu, Kaushik Bhattacharya, Andrew Stuart, and Anima Anandkumar. Fourier neural operator for parametric partial differential equations. In *Proceedings of the 9th International Conference on Learning Representations (ICLR)*, 2021. (Cited on pages 1, 2, and 7.)
- Ilya Loshchilov and Frank Hutter. SGDR: Stochastic gradient descent with warm restarts. In *Proceedings to the 5th International Conference on Learning Representations (ICLR)*, 2017. (Cited on page 7.)
- Ilya Loshchilov and Frank Hutter. Decoupled weight decay regularization. In *Proceedings to the 7th International Conference on Learning Representations (ICLR)*, 2019. (Cited on page 7.)
- Lu Lu, Pengzhan Jin, and George Em Karniadakis. DeepONet: Learning nonlinear operators for identifying differential equations based on the universal approximation theorem of operators. *arXiv preprint arXiv:1910.03193*, 2019. (Cited on pages 1 and 2.)
- Lu Lu, Xuhui Meng, Shengze Cai, Zhiping Mao, Somdatta Goswami, Zhongqiang Zhang, and George Em Karniadakis. A comprehensive and fair comparison of two neural operators (with practical extensions) based on FAIR data. *Computer Methods in Applied Mechanics and Engineering*, 393:114778, 2022. (Cited on pages 1 and 2.)
- Nicholas H Nelsen and Andrew M Stuart. The random feature model for input-output maps between Banach spaces. *SIAM Journal on Scientific Computing*, 43(5):A3212–A3243, 2021. (Cited on pages 1 and 2.)
- Adam Paszke, Sam Gross, Francisco Massa, Adam Lerer, James Bradbury, Gregory Chanan, Trevor Killeen, Zeming Lin, Natalia Gimelshein, Luca Antiga, Alban Desmaison, Andreas Kopf, Edward Yang, Zachary DeVito, Martin Raison, Alykhan Tejani, Sasank Chilamkurthy, Benoit Steiner, Lu Fang, Junjie Bai, and Soumith Chintala. PyTorch: An imperative style, high-performance deep learning library. In *Proceedings of the 33rd conference on Neural Information Processing Systems (NeurIPS)*, pp. 8024–8035. Curran Associates, Inc., 2019. (Cited on page 2.)

- Allan D Pierce. *Acoustics: An introduction to its physical principles and applications*. Springer, 2019. (Cited on page 15.)
- Md Ashiqur Rahman, Zachary E Ross, and Kamyar Azizzadenesheli. U-NO: U-shaped neural operators. *Transactions on Machine Learning Research*, 2023. ISSN 2835-8856. (Cited on pages 2 and 7.)
- Olaf Ronneberger, Philipp Fischer, and Thomas Brox. U-Net: Convolutional networks for biomedical image segmentation. In *Proceedings of the 18th International Conference on Medical Image Computing and Computer-Assisted Intervention (MICCAI)*, pp. 234–241. Springer, 2015. (Cited on pages 2 and 7.)
- Kim Stachenfeld, Drummond Buschman Fielding, Dmitrii Kochkov, Miles Cranmer, Tobias Pfaff, Jonathan Godwin, Can Cui, Shirley Ho, Peter Battaglia, and Alvaro Sanchez-Gonzalez. Learned simulators for turbulence. In *Proceedings of the 10th International Conference on Learning Representations (ICLR)*, 2022. (Cited on page 1.)
- Antonio Stanziola, Simon R Arridge, Ben T Cox, and Bradley E Treeby. A Helmholtz equation solver using unsupervised learning: Application to transcranial ultrasound. *Journal of Computational Physics*, 441: 110430, 2021. (Cited on page 2.)
- Antonio Stanziola, Simon R. Arridge, Ben T. Cox, and Bradley E. Treeby. j-Wave: An open-source differentiable wave simulator. *SoftwareX*, 22:101338, 2023. (Cited on pages 2 and 15.)
- Makoto Takamoto, Timothy Praditia, Raphael Leiteritz, Daniel MacKinlay, Francesco Alesiani, Dirk Pflüger, and Mathias Niepert. PDEBench: An extensive benchmark for scientific machine learning. *Proceedings of the 36th Conference on Neural Information Processing Systems (NeurIPS)*, 35:1596–1611, 2022. (Cited on pages 1, 2, 6, and 7.)
- Bradley E Treeby, Jiri Jaros, Alistair P Rendell, and BT Cox. Modeling nonlinear ultrasound propagation in heterogeneous media with power law absorption using a k-space pseudospectral method. *The Journal of the Acoustical Society of America*, 131(6):4324–4336, 2012. (Cited on page 15.)
- Sifan Wang, Hanwen Wang, and Paris Perdikaris. Learning the solution operator of parametric partial differential equations with physics-informed DeepONets. *Science Advances*, 7(40):eabi8605, 2021. (Cited on pages 1 and 2.)